Impact of Weather Patterns and Meteorological Factors on $PM_{2.5}$ and O_3 Responses to the Covid-19 Lockdown in China

Fuzhen Shen[1*], Michaela I. Hegglin[1,2*], Yue Yuan[3]

[1]Institute of Energy and Climate Research, IEK-7: Stratosphere, Forschungszentrum Jülich, 52425 Jülich, Germany
[2]Department of Meteorology, University of Reading, Reading, RG6 6BX, UK
[3]Jining Meteorological Bureau, Shandong 272000, China

*Correspondence to: Fuzhen Shen (f.shen@fz-juelich.de); Michaela I. Hegglin (m.i.hegglin@fz-juelich.de)

Abstract. Haze event in North China Plain (NCP) and decline in ozone levels in Southern Coast China (SC) from 21st January to 9th February 2020 during the COVID-19 lockdown have attracted public curiosity and scholarly attention. Most previous studies focused on the impact of atmospheric chemistry processes associated with anomalous weather elements in these cases, but fewer studies quantified the impact of various weather elements within the context of a specific weather pattern. To identify the weather patterns responsible for inducing this unexpected situation and to further quantify the importance of different meteorological factors during the haze event, two scenarios are employed. These scenarios implemented the comparisons of observation in 2020 with climatology averaged over the years 2015-2019 by a novel structural SOM (Self-Organising Map) model and with the prediction for 'Business As Usual' (hereafter referred to as BAU) emission strength by GBM (Gradient Boosting Machine) model, respectively. The results reveal that the unexpected $PM_{2.5}$ pollution and O_3 decline from the climatology in NCP and SC could be effectively explained by the presence of a double-centre high-pressure system across China. Moreover, the GBM results provided a quantitative assessment of the importance of each meteorological factor in driving the predictions of $PM_{2.5}$ and O_3 under the specific weather system. These results indicate that temperature played the most crucial role in the haze event in NCP, as well as in the O_3 change in SC. This valuable information will ultimately contribute to our ability to predict air pollution under future emission scenarios and changing weather patterns that may be influenced by climate change.

1 Introduction

The coronavirus disease 2019 (COVID-19) pandemic has lasted for three and half years and has led to over 6.9 million deaths globally as of June 2023 (Who, 2022). The Chinese government implemented strict lockdown measures nationwide during the first two months of 2020 to curb the spread of this pandemic (Le et al., 2020), which led to significant reductions in anthropogenic emissions, especially in the transportation sector (Xu et al., 2020; Wang et al., 2021; Liu et al., 2021). As a result, a decline not only in NO_2 but also in $PM_{2.5}$, PM_{10}, SO_2, and CO concentrations on a national scale was indicated by both satellite and ground-based measurements albeit with the negative consequence of enhancements in O_3 concentrations (Shen et al., 2022; Liu et al., 2021; He et al., 2020). Contrary to the situation in other regions from 21st January to 9th February 2020,

Northern China (NC) and Southwestern China (SWC) experienced severe haze pollution and decreased O_3 situations, respectively (Le et al., 2020; Huang et al., 2021; Wang et al., 2020). This exceptional situation, during the haze event in China thus lends itself to a large-scale 'experiment' to study the unusual phenomenon driven by atmospheric chemistry and
35　meteorology.

　　$PM_{2.5}$ and ground-level ozone (O_3), especially in highly polluted regions, adversely affect human health (Lelieveld et al., 2015), agriculture (Feng et al., 2015; Wang et al., 2007), and the Earth's radiation budget (Liao et al., 2015; Dang and Liao, 2019) thereby leading to premature mortality, decreases in crop yields, and altering the climate. Anthropogenic $PM_{2.5}$, in addition to being generated by fossil fuels and biomass burning, is also produced through the reactions of inorganics (e.g. NO,
40　NO_2, SO_2, NH_3, etc.) and Volatile-Organic Compounds (VOCs)(Zheng et al., 2017). In contrast, O_3 is not directly emitted but is formed through a series of photochemical reactions involving multiple precursors (e.g., carbon monoxide (CO), methane (CH_4), VOCs, NO, NO_2, etc.)(Ge et al., 2013). Apart from intense local primary emissions and secondary chemical formation, stagnant meteorological conditions and regional transport are two additional contributors to severe haze and O_3 pollution events (Shen et al., 2020). Recently, a series of air quality regulations (Clean Air Plans, CAPs) released by the Chinese government
45　have resulted in a notable decrease in anthropogenic emissions, leading to a substantial improvement in air quality due to reductions in $PM_{2.5}$ concentrations, but a nationwide enhancement of O_3 pollution in China (Shen et al., 2020; Li et al., 2019b). It is known that the impacts of meteorological conditions and atmospheric chemical processes could result in non-linear responses of $PM_{2.5}$ and O_3 to the decreases in their precursor concentrations (Li et al., 2019a; Li et al., 2020). However, the specific responses of air pollutants and atmospheric chemistry to emissions and meteorological conditions have not been
50　clearly determined.

　　For the haze event in China introduced above, recent studies on the topic suggested that complex atmospheric chemistry processes triggered by emission reductions and meteorological conditions are responsible for the unexpected haze formation regionally during the COVID-19 lockdown (Le et al., 2020; Fu et al., 2021). In detail, the substantial decrease in NO_2 emissions during the COVID-19 lockdown resulted in an increase in O_3 levels and nighttime NO_3 radical formation, enhancing the
55　atmospheric oxidation capacity (AOC) and facilitating the formation of secondary aerosols. Additionally, the presence of anomalous relative humidity promoted heterogeneous chemistry processes (Le et al., 2020; Huang et al., 2021; Ma et al., 2022). After the formation, more generated secondary aerosols were transported toward the in-situ measurement station in northern China (Lv et al., 2020). Meanwhile, some research pointed out that the high ambient humidity is also the key to the NC haze from the perspective of adjusting pH to control the formation efficiency of nitrate aerosol, which is one of the major species
60　for NC haze (Chang et al., 2020; Sun et al., 2020). In addition to the influence of changes in chemical reactions, a physical mechanism known as aerosol-planetary boundary layer (PBL) interaction is also considered to have had a significant impact on the haze formation (Su et al., 2020). For O_3, the decline in climatology in SC was attributable to the weakened photochemistry reactions due to the emission reductions in and the clean air masses' dilution effect on the mass loadings of NOx and VOC (Fu et al., 2021; Liu et al., 2021). Overall, meteorological conditions always played a critical role: High relative
65　humidity is the trigger of aerosol heterogeneous chemistry by adjusting the particle pH or providing a reaction medium.

Meanwhile, the transport of the secondary aerosol or clean air masses and shallow PBL height are primarily driven by wind and pressure, respectively. Importantly, the above weather elements are modulated synergistically by synoptic-scale weather patterns (SWPs) or large-scale atmospheric circulations.

Numerous studies have been conducted worldwide to explore the direct connections between SWPs and air quality Fields (Dayan and Levy, 2002; Demuzere et al., 2009; Pope et al., 2015; Hegarty et al., 2007; Bei et al., 2016; Jiang et al., 2017), indicating that good air quality conditions are often observed under cyclonic weather systems with certain types and positions, while poor air quality is frequently associated with anticyclonic conditions. However, the relationship between air quality and SWPs can differ depending on location, time and pollutants (Jiang et al., 2017; Liao et al., 2017). The methods for SWPs employed in these studies can generally be categorized into three groups: subjective (manual), mixed (hybrid), and objective (automated) (Huth et al., 2008). Objective classification methods for SWPs are known for their speed, objectivity, and high reproducibility, often achieving classification 100% automatically. On the other hand, manual approaches for SWPs have the advantage of allowing the user to control the selection of representative weather types (Lewis and Keim, 2015). Hybrid classification combines the strengths of both manual and automated techniques, where the users define the classification types, but the classification process itself is performed automatically (Frakes and Yarnal, 1997; Lewis and Keim, 2015; Huth et al., 2008). At present, the subjective method was used to investigate the contribution of six SWPs to $PM_{2.5}$ pollution in Northwest China (Bei et al., 2016). While subjective approaches are suitable for analyzing short time series, they have significant limitations when applied to large datasets spanning extended periods of time (Chen et al., 2022). Hybrid classification for SWPs is more popular than the subjective one and was applied to explore the impact of SWPs on O_3, $PM_{2.5}$ and CO in NCP, Yangtze River Delta (YRD), and Eastern China, respectively (Zhang et al., 2013; Zhang et al., 2016; Han et al., 2018; Liao et al., 2017). As an objective classification and with its advantages, the self-organising map (SOM) algorithm has been used to identify the impact of different SWPs on O_3 and $PM_{2.5}$ in YRD and Sichuan Basin (SCB), respectively (Shu et al., 2020; Zhan et al., 2019). In addition, the principle component analysis T-mode, k-mean clustering and other clustering approaches (like the Lamb-Jenkinson method) also were adopted to quantify the impact of SWPs on O_3 in NCP (Miao et al., 2017; Dong et al., 2020; Liu et al., 2019).

Based on the studies mentioned above, previous research on the drivers for unusual haze and O_3 decline events has concentrated on the influence of atmospheric chemistry processes accompanied by the anomalous of one or two weather elements, but has not yet focused on the impact of weather elements in a comprehensive and synergistic way. Therefore, we here investigate the effect of anomalies in weather conditions with respect to climatology on $PM_{2.5}$ and O_3 concentrations during the haze event in the COVID-19 lockdown, specifically. To this end, we apply a novel SOM algorithm called structural SOM (S-SOM) to identify the most meaningful clustering number of weather patterns and compare it to other traditional SOM methods including ED-SOM and the SOM algorithm based on the Pearson correlation coefficient (hereafter named COR-SOM). Furthermore, after determining the weather patterns, we evaluate the contribution of SWPs to $PM_{2.5}$ and O_3 changes during the COVID-19 lockdown in China. At last, to better understand what role each meteorological factor played in the $PM_{2.5}$ and O_3 pollution during this period, the SHapley Additive exPlanations (SHAP) approach is used to evaluate their

100 relative importance for the predictions of the Machine Learning model. The knowledge gained ultimately will help to predict air pollution under future emission scenarios and weather patterns potentially altered by climate change.

2 Method

2.1 Observational and model dataset sources

The hourly observation dataset during the first two months (January and February) from 2015 to 2020, including two air
105 pollutants ($PM_{2.5}$ and O_3) and six meteorological factors (Pressure: P, Precipitation: Precip, Temperature: Temp, Relative Humidity: RH, Wind Speed: WS, Wind Direction: WD), was divided into two parts: training dataset and test dataset, used to build a prediction model based on Machine Learning. Air pollutant and meteorological station datasets were downloaded from the National Environmental Monitoring Center (http://www.cnemc.cn) and the National Meteorological Science Data repository (https://data.cma.cn). To better understand the climatology impact on air pollutants, 367 surface measurement
110 stations across China are divided into eight different regions (including NCP: North China Plain; IM: Inner Mongolia; NEC: North Eastern China; YRD: Yangtze River Delta; CS: Central South; SC: Southern Coast; TP: Tibet Plateau; NWC: North Western China) based on different typic climate characteristics (climate classification scheme link: https://www.resdc.cn/data.aspx?DATAID=243, **Fig. 1**). Hourly surface ERA5 data with 0.25 x 0.25 spatial resolution, including Mean Sea Level Pressure (MSLP) (at 14:00 local time per day), and total Solar Radiation (SR), were retrieved from
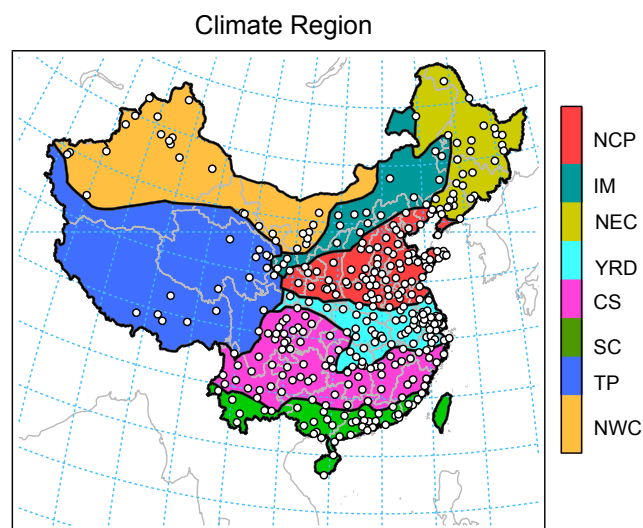115 the European Centre for Medium-Range Weather Forecasts (ECMWF).

Figure 1: The spatial distribution of air quality measurement stations in different climate regions (circles represent surface measurement stations, colors indicate different climate zones. NCP: North China Plain; IM: Inner Mongolia; NEC: North Eastern China; YRD: Yangtze River Delta; CS: Central South; SC: Southern Coast; TP: Tibet Plateau; NWC: North Western China)

2.2 Structural SOM algorithm (S-SOM)

For the SOM algorithm, it involves iterative learning processes that progressively update the nodes in the output map until they converge to a stable solution. During each learning step, the SOM algorithm selects an input vector in a random way and then searches for a node that best matches that particular vector. Traditionally, the Euclidean Distance (ED) in the SOM algorithm is often used as a criterion to search for the winning node that is closest to an input vector. ED is very popular in the SOM algorithm but with significant shortcomings when applied to compare structured inputs with temporal or spatial orders. As a result, the limitations of ED become particularly significant in climatology research, where the data are often with a spatial and temporal structure, which might result in the degradation of the spatial correlations between air pressure patterns in weather maps (Doan et al., 2021).

The S-SOM algorithm is executed following the procedure proposed by Kohoen and is widely used in many studies (Kohonen, 1982). To begin, an S-SOM is initialized by configuring the SOM node and determining the number of training iterations. The training process involves three key steps:

1. Selecting an input vector.
2. Identifying the best matching unit in the SOM for the input vector.
3. Updating the weight vectors of the SOM nodes using specific parameters.

The only difference between the traditional SOM and S-SOM is that the similarity index (S-SIM) rather than ED is used to compare the similarity between vectors. S-SOM was first proposed by Wang et al. (2004) and can be expressed in the following equation.

$$S - SOM(x, y) = \left[l(x,y)^\alpha \times c(x,y)^\beta \times s(x,y)^\gamma \right] \qquad (1)$$

Here, x, y are two vectors, and l, c, s are three comparison measurements representing luminance, contrast and structure, respectively. The three comparison functions are as follows:

$$l(x,y) = \frac{2\mu_x\mu_y + c_1}{\mu_x^2 + \mu_y^2 + c_1} \qquad (2)$$

$$c(x,y) = \frac{2\sigma_x\sigma_y + c_2}{\sigma_x^2 + \sigma_y^2 + c_2} \qquad (3)$$

$$s(x,y) = \frac{\sigma_{xy} + c_3}{\sigma_x\sigma_y + c_3} \qquad (4)$$

Here, the average and standard deviation values are represented by μ, σ, respectively. The parameters c_1, c_2, c_3 are used to stabilize division operations involving a weak denominator. The luminance, contrast, and structure in the S-SOM formula are three elements of human perception. Luminance assesses the similarity in brightness values between images. Contrast quantifies the similarity in illumination variability among images. Lastly, the structure measures the correlation in spatial interdependencies between images, reflecting how the spatial elements of the images are related to each other (Wang and

150   Bovik, 2009). Here, we can set the values of c1, c2, and c3 to 0, and the weights α, β, and γ to 1 to simplify the model (Doan et al., 2021). The final expression shows as:

$$S-\text{SOM}(x,y) = \frac{(2\mu_x\mu_y)(\sigma_{xy})}{(\mu_x^2+\mu_y^2)(\sigma_x^2+\sigma_y^2)}$$ (5)

As the function shows, the S-SOM ranges from -1 to 1. A value of 1 indicates complete similarity, while a value of -1 indicates complete dissimilarity. S-SOM offers robust, user-friendly, and comprehensible alternatives to the conventional ED approach,

155   particularly when dealing with datasets with spatial and temporal order (Wang and Bovik, 2009).

2.3 Gradient Boosting Machine (GBM) model

The impact of meteorological factors on the variation of air pollutant concentrations is typically determined via chemical transport models. However, these model predictions are associated with substantial uncertainty since they rely on the correct quantification of changes in the emission inventory of each city under multi-faceted anthropogenic air pollution interventions

160   (e.g., clean air plans, and COVID-19 lockdown measures). Besides, uncertainties can also be derived from the chemical mechanism(Knote et al., 2015; Weng et al., 2023). Here, a Gradient Boosting Machine (GBM) model was trained with observations of meteorological factors, with the GBM being able to capture the location-specific characteristics and thus suitable for the prediction of air pollutant concentrations attributable to the impact of meteorology in different cities across China. Observations of meteorological factors, together with time variables from 2015 to 2019, are considered as the training

165   dataset to predict the concentrations of $PM_{2.5}$ and O_3 in China. The meteorological factors are listed as follows: P, Precip, Temp, RH, WS, and WD. The time variables include Julian Day (JD), Day of Week (DOW), Holidays, and the Chinese New Year (CNY) days in each year. For the GBM prediction model, cross-validation is mainly used to estimate how accurately a predictive model will perform in practice. To check the accuracy of the ML model used in our study, a time series split rolling cross-validation based on 5 splits was used, for which data used for the training task always preceded the data used for

170   validation. In detail, the ML training model was used for 2015, 2015-2016, 2015-2017, 2015-2018, and 2015-2019, while the testing of the model then was implemented over the first two months of 2016, 2017, 2018, 2019, and 2020, respectively(Shen et al., 2022). The hyperparameters of the model that we selected are as follows: 'number_leaves ', 'objective', 'min_data_in_leaf', 'learning_rate', 'feature_fraction', 'bagging_fraction', 'bagging_freq', and 'metric' (detailed parameter information of the model can be accessed from: https://lightgbm.readthedocs.io/en/latest/Parameters.html). After selecting the

175   best Machine Learning (ML) model under cross-validation, a ML experiment was designed to make a prediction of $PM_{2.5}$ and O_3 in the first two months of 2020.

2.4 Shapley Additive ExPlanation (SHAP) Method

Quantifying the importance of input features of the GBM model is as vital as the overall accuracy of the prediction itself. However, interpreting the higher accuracy achieved by ensemble or ML models on certain datasets can be a challenging task.

180   To deal with this contradiction between higher accuracy and non-interpretability, SHAP, a game theory approach, is applied

to calculate the importance value for each specific independent feature. In brief, the SHAP value of each feature is attributed to the difference in one prediction output with one feature versus the prediction output without this corresponding feature. SHAP's local explanations can vary in being positive or negative, reflecting how predictors influence the predicted outcome. In contrast, other ML methods typically yield a single positive value, indicating overall importance. Specifically, in local interpretability analysis(Lundberg et al., 2020), SHAP indicates the contribution of each variable to the prediction of a specific sample. This contribution is assessed from the base value (the predicted mean value) to the final model output. Variables that push the prediction to higher values are displayed in positive, while those decreasing the prediction are shown in negative. For each predicted model with n variables in one sample (x_l) and the predicted output $f(x_l)$, the equation of the prediction function is described as follows:

$$f(x_l) = E_0(f, x) + \sum_{m=1}^{n} E_m(f, x_l) \tag{6}$$

where x_l is the input with variable m in the prediction model f generating the SHAP value of $E_m(f, x_l)$. $E_0(f, x)$ is the expected value for the prediction model over the whole dataset.

3 Results

3.1 Spatial variations of air pollutant and meteorology in climatology

The spatial distribution of the fractional differences in air pollutant concentrations during the haze event from 21st Jan to 9th Feb 2020, calculated between mean values during the event in 2020 and the values averaged over the same period from 2015 to 2019, for all six air pollutants are shown in **Fig. 2**. Half of the climate regions, including YRD, CS, SC, and TP, showed different magnitudes in decreases (increases) (**Table 1**) from the climatology for $PM_{2.5}$, PM_{10}, NO_2, SO_2, and CO (O_3), primarily attributed to the significant anthropogenic emission reduction during the COVID-19 lockdown (Nie et al., 2021; Wang et al., 2022; Shen et al., 2022). However, contrary to expectations, $PM_{2.5}$ concentrations did not drop as anticipated at the beginning of the lockdown in NCP, IM, NEC and NWC. Instead, these regions experienced an unexpected increase of 8.6%, 31.8%, 22.3%, and 2% compared to climatology during the same period, respectively. Even though the decline was small, O_3 showed an unexpected drop of -0.8% in SC when compared to climatology during the same period. Our recent work also found a -0.9% decline in O_3 driven by the meteorological effect during the COVID-19 lockdown across China (Shen et al., 2022). As a fractional difference from climatology, the spatial distribution of the key meteorological variables RH, P, Precip, Temp, and WS are shown in **Fig. 3**. Generally, positive RH and negative WS anomalies are always accompanied by strong regional elevation of $PM_{2.5}$ in NCP, NEC, IM, and NWC. Positive P anomalies coupled with increased $PM_{2.5}$ demonstrate the most prominent regional characteristics in NEC. In SC, the most noticeable features were observed as a combination of hotspot Precip anomalies and decreased O_3 levels. Overall, the regional characteristics of $PM_{2.5}$ and O_3 all have a close relationship with different meteorological anomalies, which are usually controlled by the regionally prevailing SWP.
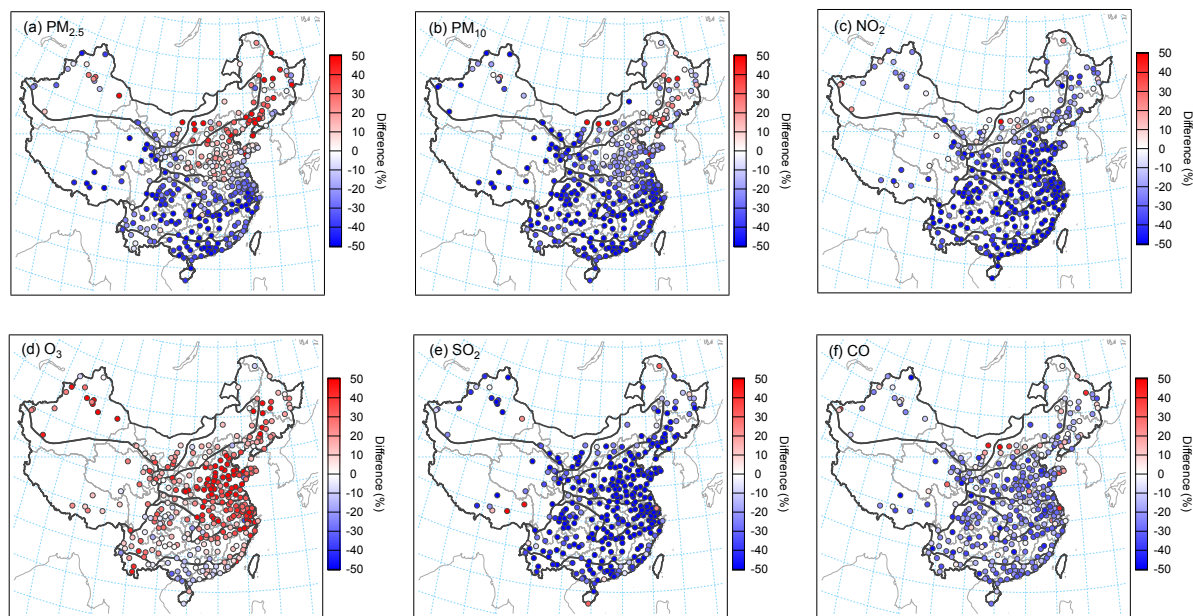
Figure 2: The spatial distributions of fractional differences between mean values during the haze event in 2020 and the climatology over the same period of the years 2015-2019 for six air pollutants (including PM$_{2.5}$, PM$_{10}$, NO$_2$, O$_3$, SO$_2$, and CO).
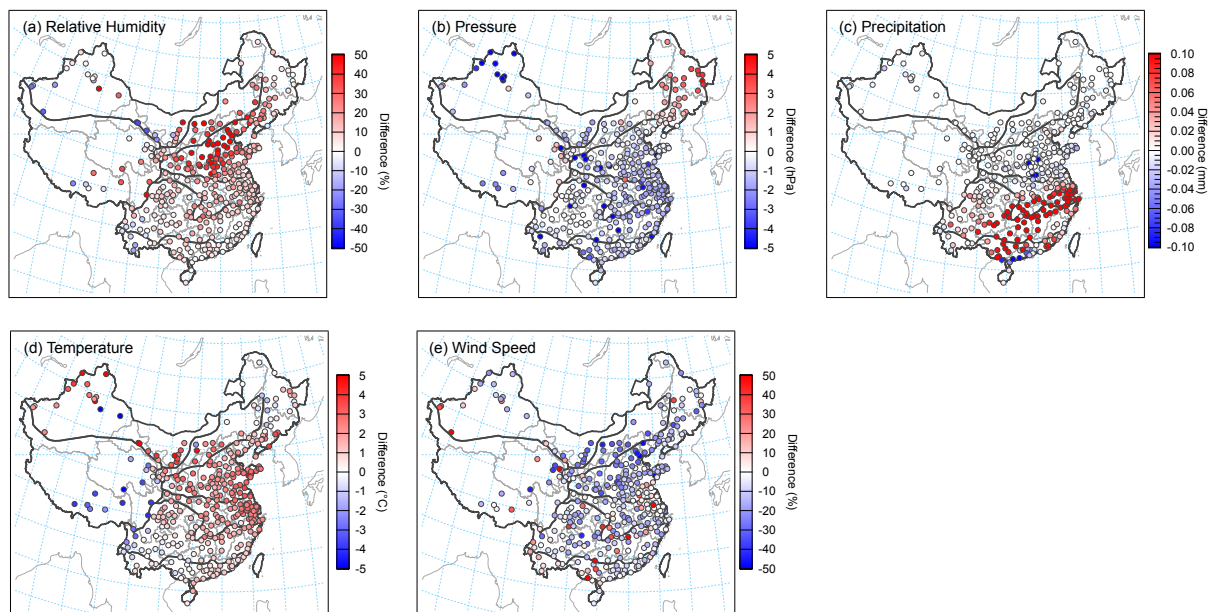

Figure 3: The spatial distributions of differences between mean values during the haze event in 2020 and the climatology over the same period of the years 2015-2019 for meteorological factors (including Relative Humidity, Pressure, Precipitation, Temperature, and Wind Speed).

Table 1. The climate zones and mean fractional climatology anomalies (2020-mean(2015-2019)) of six air pollutants across China.

| Climate zone	Number of cities	Climate characteristics	$PM_{2.5}$	PM_{10}	O_3	NO_2	SO_2	CO
NCP	86	Semi-humid warm temperate climate	8.6%	-17.6%	39.3%	-43.4%	-66.9%	-23%
IM	17	Semi-arid mid-temperate climate	31.8%	-10.7%	15%	-9.4%	-40.2%	-2.6%
NEC	31	Cold temperate climate, semi-humid, mid-temperate climate	22.3%	0.7%	26.4%	-24.2%	-45.8%	-10.3%
YRD	67	Humid, north subtropical climate	-29.7%	-41.7%	32.4%	-54.3%	-60.9%	-24.6%
CS	68	Humid, mid-subtropical climate	-41.4%	-50.9%	11.5%	-53.2%	-56.7%	-25.2%
SC	42	South subtropical climate	-40.2%	-45.2%	-0.8%	-51.8%	-44.3%	-24.8%
TP	9	Plateau climate	-48%	-61.9%	16%	-27.3%	-40.1%	-26.4%
NWC	28	Arid, mid-arid, mid-temperate climate	2%	-34.1%	28.7%	-14.5%	-49.6%	-12.3%

3.2 Identification of the SWP during the unexpected haze event

To identify which SWP can regionally induce an unexpected $PM_{2.5}$ increase and O_3 reduction compared to climatology averaged over the years 2015-2019, three different SOM methods were employed to identify different types of SWPs (from 2 to 8) by using MSLP data in the first two months from 2015 to 2020 over China. **Fig. 4** shows MSLP patterns identified by S-SOM, COR-SOM, and ED-SOM running three nodes, respectively. Taking this three-node analysis as an example, we can find that the three SWPs identified by S-SOM (**Figs. 4a, 4b, and 4c**) are clearly distinct from each other. On the other hand, ED-SOM (**Figs. 4d and 4e**) and COR-SOM (**Figs. 4g and 4h**) both classify two similar SWPs characterised by high-pressure systems over Siberia, thus resulting in a failure of clustering. This interpretation is supported by the result of clustering number

distributions for the three-node SWPs (**Fig. 5d**). It should be noted that cluster numbers do not necessarily correspond to the same pattern between S- / ED-/ COR-SOM. Here, it is found that S-SOM results are in a more 'ordered' clustering of nodes, where a prominent node (62.9%) is accompanied by two non-dominant nodes (7.5% and 29.5%). On the other hand, both ED-SOM and COR-SOM exhibit relatively similar cluster sizes with a percentage of 27%, 35.1%, and 37.9% for ED-SOM and 40.7%, 34.6%, and 24.7% for COR-SOM, highlighting the prevalence of a more 'flat' clustering pattern. It can be concluded that the better classification method for three-node SWPs is S-SOM with an 'ordered' clustering number distribution accompanied by a prominent node (Doan et al., 2021). This consistent finding is also observed in other cases (**e.g. node numbers smaller or greater than 3,**
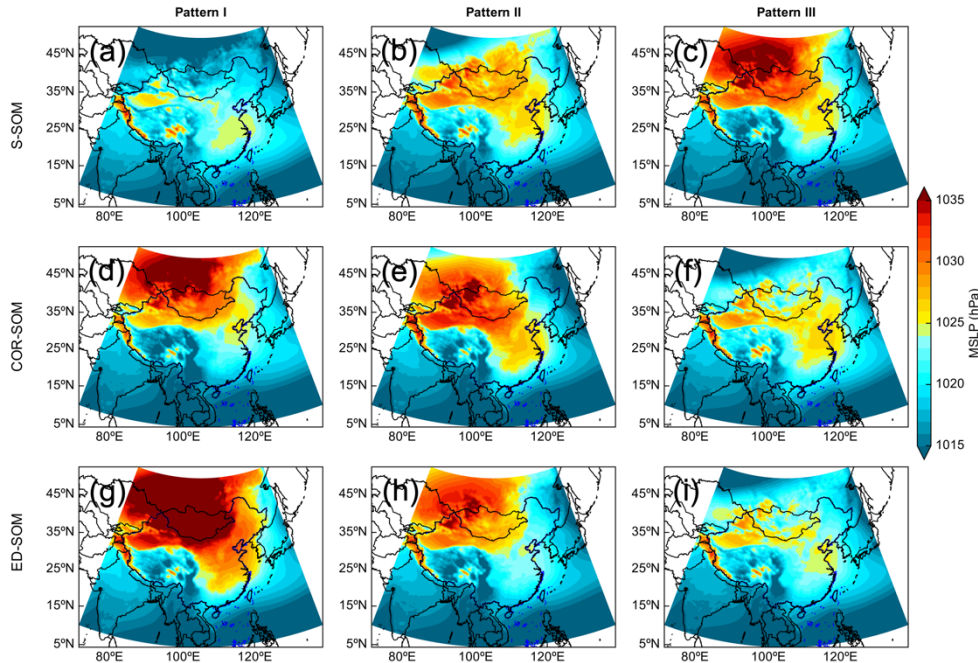
Figure 4: Spatial distributions of three weather patterns for MSLP (Mean Sea Level Pressure) identified by S-SOM (a, b and c), COR-SOM (d, e, and f), and ED-SOM (g, h, and i) during the first two months from 2015 to 2020.
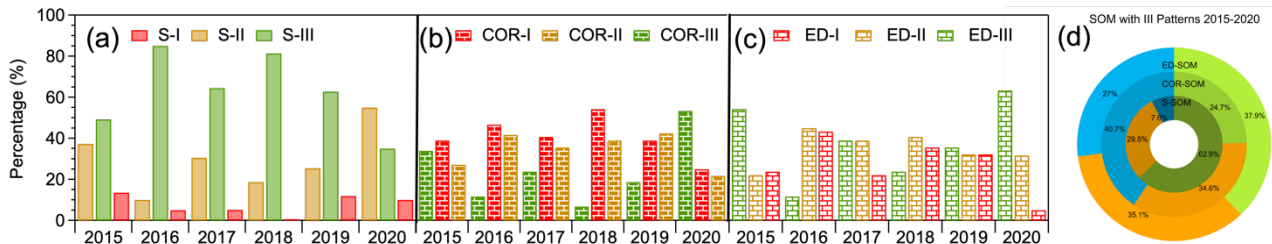

Figure 5: Cluster size distributions identified by S-SOM (inner ring), COR-SOM (middle ring) and ED-SOM (outer ring) over the years 2015-2020 (d) and cluster days in each year (a: S-SOM; b: COR-SOM; c: ED-SOM).

Fig. S1-S12). Then, we make a further comparison of the node number distribution of S-SOM (**Fig. 5a**), ED-SOM (**Fig. 5b**), and COR-SOM (**Fig. 5c**) in each year and find that S-SOM always has a prominent node with a value of more than 50% (2015:50%, 2016: 85%, 2017: 64%, 2018: 81%, 2019: 63%, and 2020: 55%) and the cluster sizes for ED-SOM and COR-SOM are close to each other as well, which is consistent with a recent study indicating a better performance of S-SOM (Doan et al., 2021). Therefore, in addition to the algorithmic advantages, the characteristics of 'ordered' clustering nodes reinforce the superiority of the S-SOM approach.

In terms of structure characteristics of clustering number distribution for S-SOM, three-node SWPs (**Fig. 4**) and seven-node SWPs (**Fig. S13**) were regarded as the optimal numbers of SWPs after checking the clustering number distribution for each run. From the top panel of **Fig. 4**, three types of SWPs identified by S-SOM demonstrate that NCP, YRD, NEC and NWC are under the control or influence of different high-pressure systems. For seven-node SWPs identified by S-SOM, even though the high-pressure system varies in numbers and locations, some patterns (**Fig. S13d and Fig. S13e**) still have a relatively high similarity, which might be attributed to the over-splitting or a too-short dataset to capture the full climatology. Overall, the result of three-node SWPs of S-SOM is thus identified as the best solution to study the haze event in China in further detail.

## 3.3 Impact of weather elements on PM2.5 and O3 under the SWP

To better understand the regional influence of different SWPs on $PM_{2.5}$ and O_3 concentration levels, NCP and NEC (SC), which have higher (lower) than expected concentrations for $PM_{2.5}$ (O_3) and have more measurement stations as well, were selected as the research domains, respectively. To investigate the cause of the unexpected $PM_{2.5}$ and O_3 variations with respect to climatology, a comparison of identified three-node SWPs is made between the days of 2020 and 2015-2019. As is shown in **Fig. 6** and as detailed in **Figs. 7-9**, pattern-I in 2020 (**Fig. 6d**) shows a North Coastal high-pressure circulation system, located in the Yellow Sea, which is enhanced from that in 2015-2019 (**Fig. 6a**) and influences the NCP and NEC regions (see **Figs. 7a,d-f and 8a,d-f**) more strongly from the southeast direction with a generally warmer and, in the case of NEC, also faster airflow. The double-centre high-pressure system in pattern-II is strengthened in 2020 (**Fig. 6e**) and located in the region of Mongolia and the Bohai Sea in China compared to 2015-2019 (**Fig. 6b**). This brings along a more stagnant, that is low-speed and cold, but in addition extremely wet, northern airflow controlling the NCP region (**Figs. 7a,d-f**) and a moderately wetter airflow dominating the NEC region (**Figs. 8a,d-f**). Pattern-III, on the other hand, shows a much weakened Siberian high and a missing China north coastal high in 2020 (**Fig. 6f**), when compared to a pattern exhibiting two high-pressure centres during the 2015-2019 reference period (**Fig. 6c**). This leads to a generally warmer, slightly faster, and more humid airflow to the NCP (**Figs. 7a,d-f**) and NEC (**Figs. 8a,d-f**) regions. For SC, which is always located at the most southern part of the observed high-pressure centres (**Fig. 6**), and for all three patterns, only small changes are seen in 2020 compared to the 2015-2019 time period with a more easterly component in winds (**Figs. 9a-c**), leading to slightly warmer and (except for pattern III) moister airflow (**Figs. 9 d-f**).
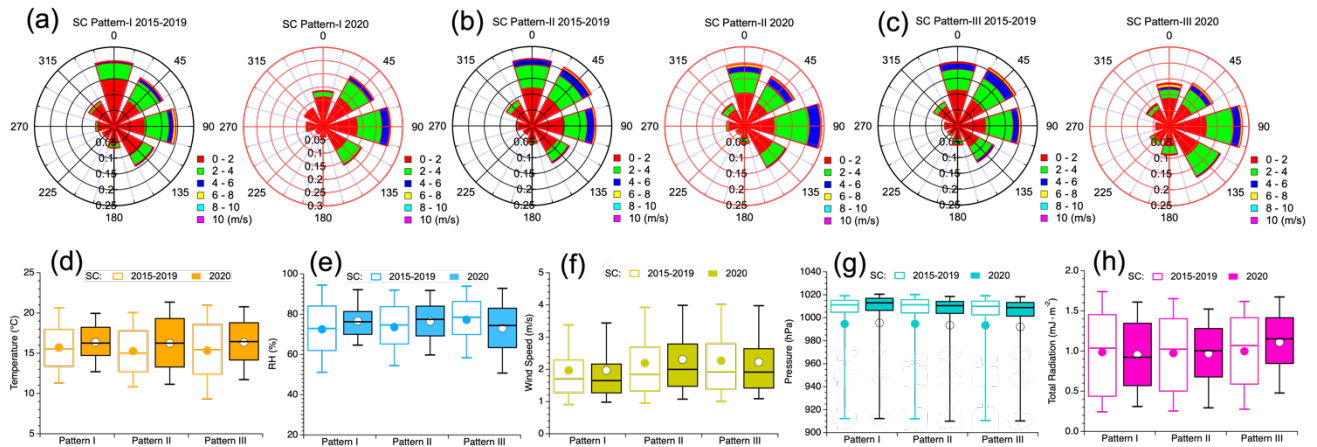
11
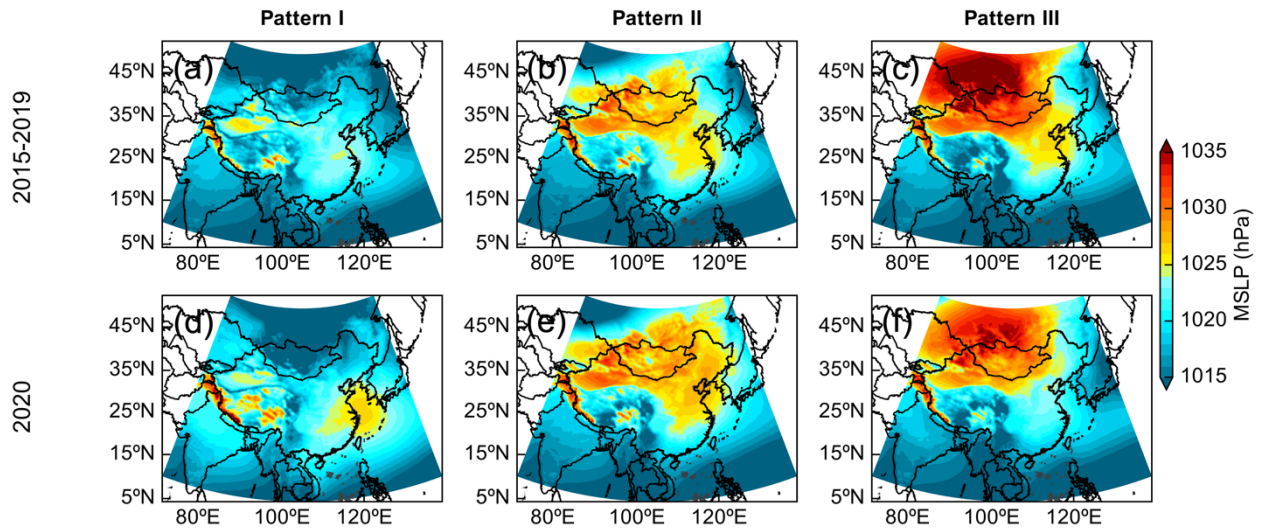
Figure 6: Comparison of the three weather patterns between cluster days in 2020 (d, e, and f) and 2015-2019 (a, b, and c), respectively.
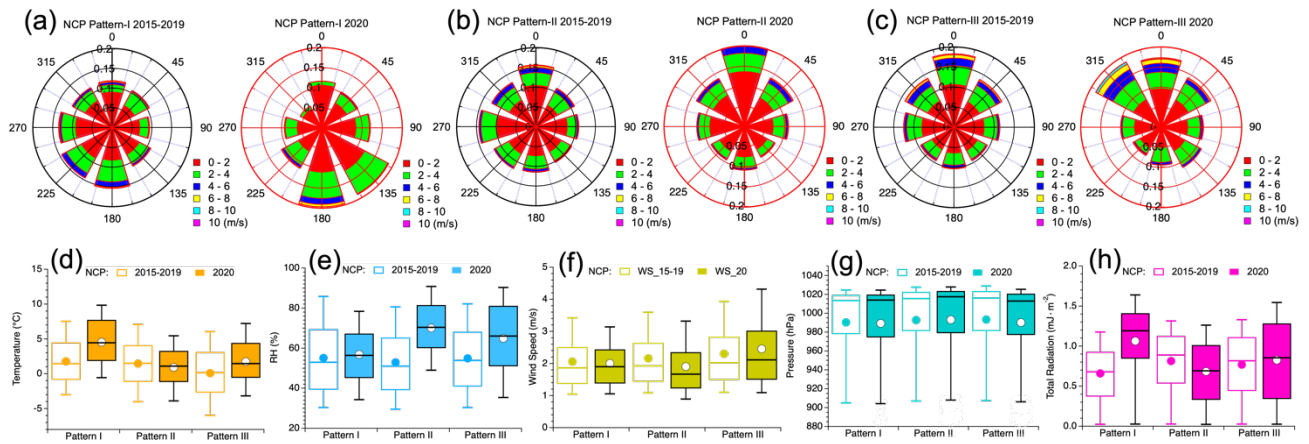
Figure 7: Comparisons of different weather factors (including Wind Speed, Wind Direction, Temperature, Relative Humidity, Pressure, and Total Radiation) between cluster days in 2020 (red rings and solid whisker-boxes) and in 2015-2019 (black rings and hollow whisker-boxes) for the three weather patterns in NCP.

12
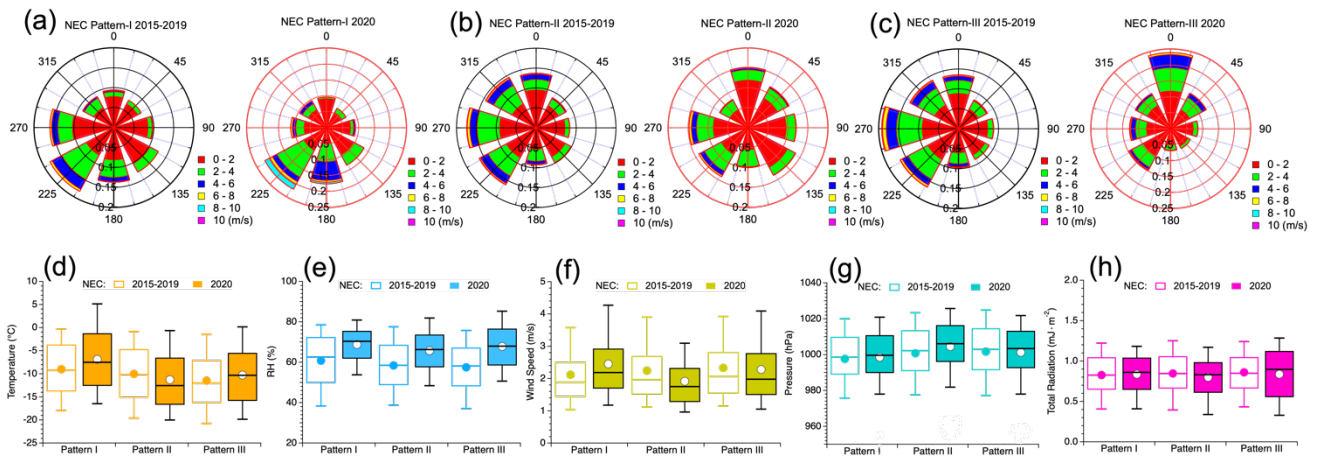
Figure 8: Comparisons of different weather factors (including Wind Speed, Wind Direction, Temperature, Relative Humidity, Pressure, and Total Radiation) between cluster days in 2020 (red rings and solid whisker-boxes) and in 2015-2019 (black rings and hollow whisker-boxes) for the three weather patterns in NEC.

Figure 9: Comparisons of different weather factors (including Wind Speed, Wind Direction, Temperature, Relative Humidity, Pressure, and Total Radiation) between cluster days in 2020 (red rings and solid whisker-boxes) and in 2015-2019 (black rings and hollow whisker-boxes) for the three weather patterns in SC.

We now turn to the discussion of the observed distributions of $PM_{2.5}$ and O_3 (**Fig. 10**) aggregated over the three SWPs and the regions NCP, NEC, and SC for the 2020 and the 2015-2019 time periods, respectively. For $PM_{2.5}$ in NCP (**Fig. 10a**), the mean values in pattern-I, II, and III in 2015-2019 all remained at high pollution levels with a value of 96.4, 92.6, and 87.7 $\mu g/m^3$, respectively. In contrast, due to the anthropogenic emissions reductions during the lockdown period in 2020, the $PM_{2.5}$ mean values for patterns I and III decreased to 68.8 and 59.8 $\mu g/m^3$ even coupled with a positive RH climatological anomaly (**Fig. 7e**: 2% and 10%), which could be conducive to generating additional $PM_{2.5}$ generally. Unlike pattern-I and III, the $PM_{2.5}$ mean value in pattern-II 2020 surprisingly keeps at an equivalent level (92.5 $\mu g/m^3$) to pattern-II in 2015-2019 (92.6 $\mu g/m^3$) under a weather condition of a combination of the greatest RH anomaly (**Fig. 7**: 17%) and a negative WS anomaly (**Fig. 7f**:

13

-0.3 m/s), which offsets the contribution from the emissions reduction in NCP. For O_3 in NCP (**Fig. 10d**), the pattern-I and -III in 2020 exhibit greater temperature anomalies (**Fig. 7d**: 2.7 °C and 2.9 °C; consistent with higher total radiation levels, see **Fig. 7h**) and thus facilitate additional O_3 generation (20 µg/m^3 and 13 µg/m^3). The pattern-II in 2020 with a negative temperature anomaly (-0.1 °C; consistent with lower total radiation levels, see **Fig. 7h**) is favouring to a more moderate O_3 increase (3 µg/m^3).
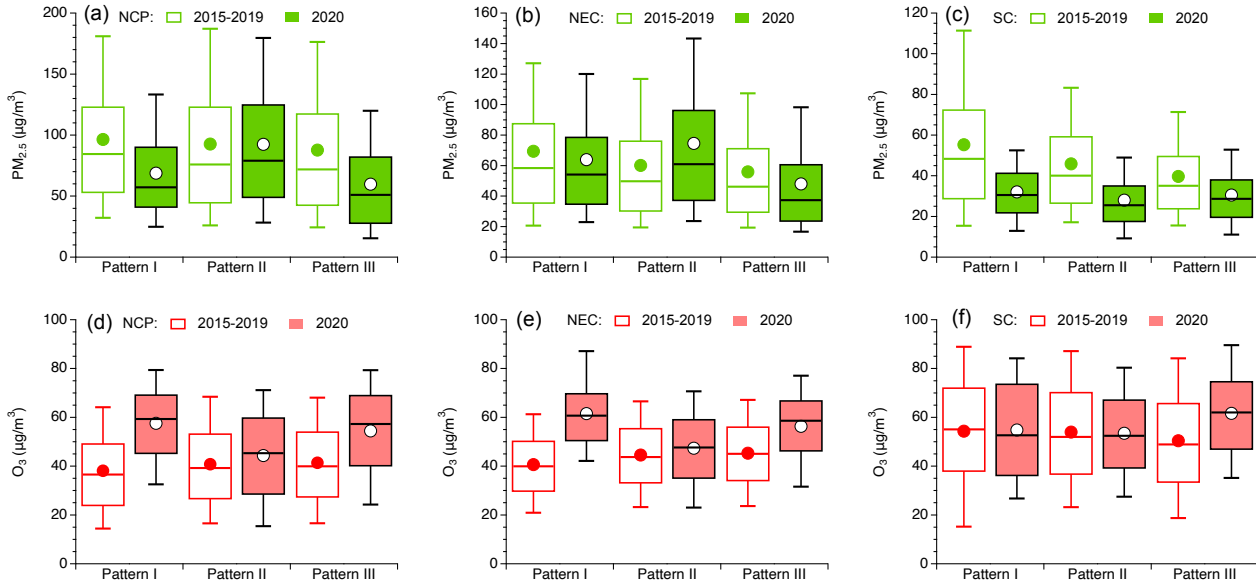

Figure 10: Comparisons of PM$_{2.5}$ (green colour) and O$_3$ (red colour) between cluster days in 2020 (filled whisker-boxes) and in 2015-2019 (hollow whisker-boxes) for the three weather patterns in NCP (a and d), NEC (b and e), and SC (c and f).

In the NEC region, the maximum PM$_{2.5}$ increase (15 µg/m^3) occurred under the influence of pattern-II in 2020(**Fig. 10b**), with a negative wind speed anomaly (**Fig. 8f**: -0.3 m/s) when compared to the same pattern in 2015-2019, indicating the meteorological effect acts in the opposite way to the emission reductions during the COVID-19 lockdown period. Whilst, without an offset effect from the unfavourable meteorological conditions, mean values of PM$_{2.5}$ for pattern-I and III in 2020 decreased by 5 µg/m^3 and 8 µg/m^3, respectively. For O_3 (**Fig. 10e**), unlike a negative temperature anomaly (**Fig. 8d**: -1.3 °C) in SWP-II, both higher O_3 increases in SWP-I (11 µg/m^3) and III (11 µg/m^3) than that in SWP-II (2 µg/m^3) are driven by positive temperature anomalies (**Fig. 8d**: 2 °C and 4.4 °C).

In the SC region, without an extreme weather element anomaly facilitating additional PM$_{2.5}$ production, PM$_{2.5}$ mean values for all three SWPs in 2020 are at a lower level than in 2015-2019 (**Fig. 10c**), attributable to the emissions reductions during the COVID-19 lockdown. Higher precipitation levels in 2020 than during the 2015-2019 period also helped reduce PM$_{2.5}$ levels (see **Figs. 3c and S14**). For O_3 (**Fig. 10f**), a negative RH anomaly (**Fig. 9e**) for SWP-III in 2020 has led to the greatest O_3 elevation for this region. On the other hand, O_3 in pattern-I is found to remain at similar levels during both time periods since no significant differences in weather patterns are found. Finally, a positive wind speed anomaly (**Fig. 9f**: 0.21m/s) is

conducive to an unusual O_3 decline (-0.5 µg/m³) in SWP-II in 2020 when compared to 2015-2019, which is contrary to the O_3 situation under the effect of all other SWPs discussed above.

330   Overall, we found that the unexpected $PM_{2.5}$ pollution increase in NCP and NEC and an O_3 decline in SC occur simultaneously only during SWP-II, which is equivalent to the situation found in the observations during the haze event. When we further investigate the calendar occurrences of the three different SWPs (**Fig. S15**), it is indeed found that 70% of haze days were associated with SWP-II. This finding thus indicates that SWP-II can be regarded as the representative weather pattern which best explains the cause of the unexpected haze and O_3 decline events.

335 **3.4 Predominant meteorological factors for $PM_{2.5}$ and O_3 pollution**

After identifying which SWP could control the impact of each weather element on $PM_{2.5}$ and O_3 levels as observed during the haze event in 2020, we further use machine learning coupled with the SHAP approach to quantify the impact of each weather element on the $PM_{2.5}$ and O_3 under 'Business As Usual' (hereafter referred to as BAU) emission strength scenario during the haze event in 2020. This BAU scenario thereby is constructed by the Gradient Boosting Machine that trained the model by

340   using historical features to predict the future dependent features without considering the huge emission reduction due to the COVID-19 lockdown. It is a counterfactual scenario assuming the emission strength is the same as the BAU. In our previous study, the GBM model was applied to train daily data over 2015-2019 and predict six air pollutants including $PM_{2.5}$ and O_3 over the first three months of 2020 in 367 cities across China (Shen et al., 2022). The good performance of the GBM model was measured by achieving relatively high Pearson Correlation Coefficients (PCC) and lower root-mean-squared errors

345   (RMSE) for the final predictions of $PM_{2.5}$ and O_3 (the details can be found in the supplementary materials). **Fig. 11 (a), (d), and (g)** and **Fig. S16** show the time series results in the first two months for $PM_{2.5}$ and O_3 between the observation and prediction in NCP, NEC, and SC respectively. We find that the predictions agree generally well with the observations with reasonably high PCCs (NCP: 0.7, NEC: 0.6, SC: 0.8), indicating the good performance of the GBM model. Note that these predictions might be with high Root Mean Square Errors (RMSEs) due to the input being the BAU emissions instead of the

350   lockdown emission reduction. Many studies have estimated $PM_{2.5}$ and O_3 by using different prediction models, but they are limited to explain the final predictions(Xiao et al., 2018; Zhang et al., 2021; Jin et al., 2022), especially to provie details of specific input features(Weng et al., 2022). In our study, the SHAP module coupled to the GBM model was run to quantify the importance of the input variables during the haze event in 2020 (**Fig. 11 (b), (e), and (h)**). On average, in the BAU scenario, the SHAP value of time variables, including CNY, DOW, Holiday, and Julian Day, have no or negative impacts on $PM_{2.5}$ and

355   O_3 (**Fig.11(c), (f), and (i)**). For meteorological elements that enhanced the production of $PM_{2.5}$, temperature ranked first among the six meteorological elements during the haze event, followed by RH, WS and pressure in NCP, versus WS, pressure and RH in NEC respectively. In terms of the positive SHAP values of temperature, pressure, RH, and WS in $PM_{2.5}$ predictions, it reveals that those meteorological features push $PM_{2.5}$ prediction to a higher value, suggesting the final predictions were up to the baseline concentrations in NCP and NEC. In SC (**Fig. 11(i))**, positive mean SHAP values (2.2 µg/m³) for RH would be

360   conducive to additional ozone generation due to the relative lower values compared to the before haze event (**Fig. 11(g)),** thus

pushing the predicted ozone higher. In contrast, negative mean SHAP value (-5.5 µg/m³) for temperature during the haze event (**Fig. 11(i)**) would suppress ozone production attributable to smaller mean values thus leading to a lower ozone prediction. It should be noted that RH with a higher absolute SHAP value (9.8 µg/m³) exceeding temperature (-6.7 µg/m³) became the primary factor dominating the high ozone level from 27th Jan to 2nd Feb 2020. It is attributed to the SWP-II in SC (*Fig. 9(d, f)*) with strong moist winds from the ocean, leading to the importance of RH surpassing temperature, which is consistent with the previous study (Weng et al., 2022). However, over the full period of the haze event, the negative effect of temperature dominated a higher ozone level during the haze event based on the larger absolute SHAP value for temperature. This non-decreased response from ozone to lower temperature might be attributed to the uncoordinated emission reductions of ozone precursors. When we investigate the observed weather elements in 2020 against that averaged over 2015-2019, we can find that NCP and NEC were both under the control of SWP-II with lower temperatures and a higher RH, which facilitate the formation of PM₂.₅. Meanwhile, the SC region was influenced by the SWP-II with higher temperatures, higher RH and higher WS weather conditions, resulting in a decline of O₃ in climatology but a relative high ozone level in prediction from the SHAP explanation. Overall, we could not only find the impact of weather elements on PM₂.₅ and O₃ in the prediction scenario and in climatology, but also can conclude that temperature plays a key role in such an impact.
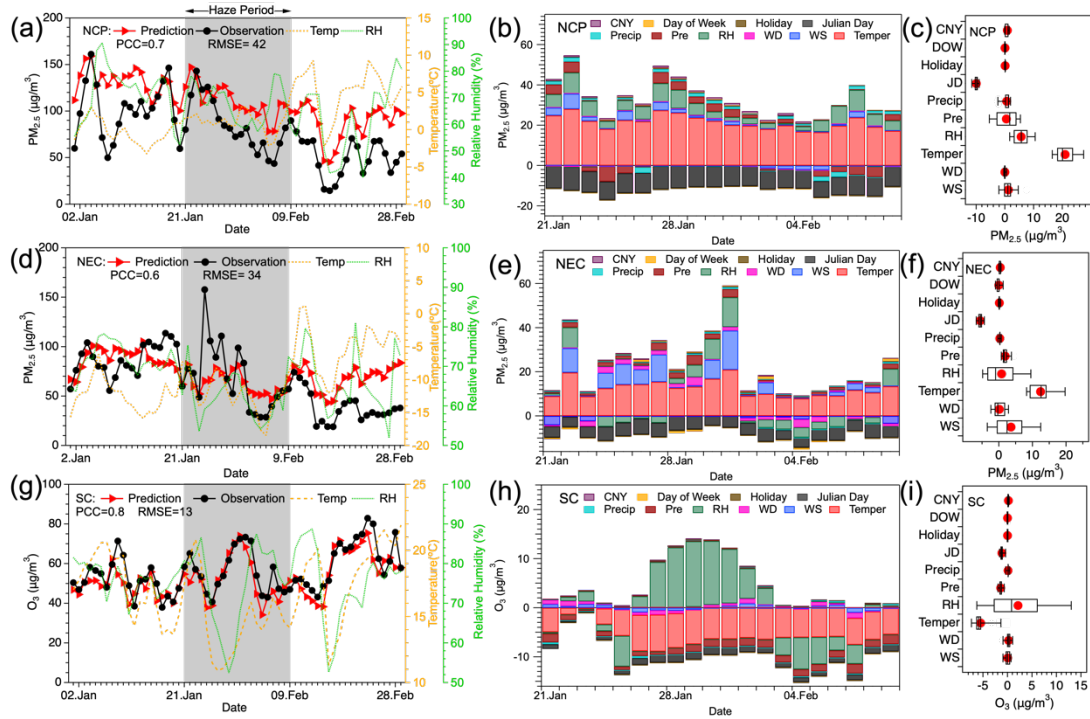

Figure 11: Time series comparisons between observations (black dot line) and predictions (red triangle line) combined with the SHAP values of the input variables (colourful bar) for the PM₂.₅ and O₃ predictions in NCP (a and b), NEC (d and e), and SC (g and h) respectively (Note that the whisker-box plots represent the mean SHAP value of the input variables during the prediction in NCP (c), NEC (f), and SC (i) respectively and shaded area (a, d, g) indicates the haze event period).

4 Conclusion

At the beginning of the COVID-19 pandemic, China suspended almost all non-essential human activities. However, serious haze pollution still occurred in North China during this period, triggering extensive investigations. On the other hand, whilst O_3 concentrations were increasing across almost all of China due to the shift in the chemical regime, the SC region exhibited a decrease in O_3. To further understand the role of meteorology in regulating air pollution during this period, we investigated in more detail the role of synoptic-scale weather patterns in driving the meteorology in these regions of China. To this end, we first determined the optimal approach for identifying synoptic-scale weather patterns out of three self-organising map methods. With the S-SOM method yielding the most optimal results, we then analysed the variation of each meteorological factor under the control of the weather type that produces anomalous $PM_{2.5}$ concentrations in the NCP and NEC, and anomalous O_3 concentrations in SC, and finally quantify the importance of each meteorological factor assuming a BAU scenario through a machine-learning model coupled with a SHAP module.

The large-scale double centre high-pressure system was identified by the optimal S-SOM method, which is with low-speed-cold-extremely wet-northern airflow controlling the NCP region, with low-speed-warm-wet airflow from the Bohai Sea dominating the NEC region, and with warmer air masses covering the SC region simultaneously. Whilst, the above weather elements anomalies controlled by the large-scale high pressure could well explain the unexpected $PM_{2.5}$ pollution and O_3 decline in climatology in NCP, NEC, and SC respectively.

Moreover, the SHAP results indicate that in the BAU scenario, the time series trend of $PM_{2.5}$ and O_3 have a high similarity with that of observations, indicating a good performance of the prediction model (despite the differing emissions). The SHAP results stress the impact of meteorological conditions on $PM_{2.5}$ and O_3 and further quantify the importance of each weather element under the specific weather system, revealing the most important role that temperature played in $PM_{2.5}$ pollution in NCP and NEC, and in high O_3 level (albeit, note that this has to be understood relative to a lower ozone level compared to climatology) in SC, respectively.

Overall, this study provides a potential way to understand the synergistic effects of various meteorological factors in reducing pollution and to quantify the importance of each weather element as well. As a result, the provision of information on what role each weather element plays in unexpected air pollution cases can help policymakers to implement air pollution control strategies. However, our work will have to be expanded further and add more related meteorological factors to GBM model to improve its performance. In fact, more studies should focus on the topic of understanding the impact of meteorology on different air pollutants in particular due to weather conditions in a changing climate.

References

Bei, N., Li, G., Huang, R. J., Cao, J., Meng, N., Feng, T., Liu, S., Zhang, T., Zhang, Q., and Molina, L. T.: Typical synoptic situations and their impacts on the wintertime air pollution in the Guanzhong basin, China, Atmos. Chem. Phys., 16, 7373-7387, 10.5194/acp-16-7373-2016, 2016.

Chang, Y., Huang, R.-J., Ge, X., Huang, X., Hu, J., Duan, Y., Zou, Z., Liu, X., and Lehmann, M. F.: Puzzling Haze Events in China During the Coronavirus (COVID-19) Shutdown, Geophys. Res. Lett., 47, e2020GL088533, https://doi.org/10.1029/2020GL088533, 2020.

Chen, X., Wang, N., Wang, G., Wang, Z., Chen, H., Cheng, C., Li, M., Zheng, L., Wu, L., and Zhang, Q.: The influence of synoptic weather patterns on spatiotemporal characteristics of ozone pollution across Pearl River Delta of southern China, Journal of Geophysical Research: Atmospheres, 127, e2022JD037121, 2022.

Dang, R. and Liao, H.: Radiative forcing and health impact of aerosols and ozone in China as the consequence of clean air actions over 2012–2017, Geophys. Res. Lett., 46, 12511-12519, 2019.

Dayan, U. and Levy, I.: Relationship between synoptic-scale atmospheric circulation and ozone concentrations over Israel, Journal of Geophysical Research: Atmospheres, 107, ACL 31-31-ACL 31-12, 2002.

Demuzere, M., Trigo, R. M., Vila-Guerau de Arellano, J., and van Lipzig, N. P. M.: The impact of weather and atmospheric circulation on O_3 and PM_{10} levels at a rural mid-latitude site, Atmos. Chem. Phys., 9, 2695-2714, 10.5194/acp-9-2695-2009, 2009.

Doan, Q. V., Kusaka, H., Sato, T., and Chen, F.: S-SOM v1.0: a structural self-organizing map algorithm for weather typing, Geosci. Model Dev., 14, 2097-2111, 10.5194/gmd-14-2097-2021, 2021.

Dong, Y., Li, J., Guo, J., Jiang, Z., Chu, Y., Chang, L., Yang, Y., and Liao, H.: The impact of synoptic patterns on summertime ozone pollution in the North China Plain, Sci. Total Environ., 735, 139559, https://doi.org/10.1016/j.scitotenv.2020.139559, 2020.

Feng, Z., Hu, E., Wang, X., Jiang, L., and Liu, X.: Ground-level O3 pollution and its impacts on food crops in China: a review, Environ. Pollut., 199, 42-48, 2015.

Frakes, B. and Yarnal, B.: A procedure for blending manual and correlation-based synoptic classifications, International Journal of Climatology, 17, 1381-1396, https://doi.org/10.1002/(SICI)1097-0088(19971115)17:13<1381::AID-JOC204>3.0.CO;2-Q, 1997.

Fu, S., Guo, M., Fan, L., Deng, Q., Han, D., Wei, Y., Luo, J., Qin, G., and Cheng, J.: Ozone pollution mitigation in guangxi (south China) driven by meteorology and anthropogenic emissions during the COVID-19 lockdown, Environ. Pollut., 272, 115927, https://doi.org/10.1016/j.envpol.2020.115927, 2021.

455 Ge, B., Sun, Y., Liu, Y., Dong, H., Ji, D., Jiang, Q., Li, J., and Wang, Z.: Nitrogen dioxide measurement by cavity attenuated phase shift spectroscopy (CAPS) and implications in ozone production efficiency and nitrate formation in Beijing, China, Journal of Geophysical Research: Atmospheres, 118, 9499-9509, 2013.

Han, H., Liu, J., Yuan, H., Jiang, F., Zhu, Y., Wu, Y., Wang, T., and Zhuang, B.: Impacts of synoptic weather patterns and their persistency on free tropospheric carbon monoxide concentrations and outflow in eastern China, Journal of Geophysical
460 Research: Atmospheres, 123, 7024-7046, 2018.

He, G., Pan, Y., and Tanaka, T.: The short-term impacts of COVID-19 lockdown on urban air pollution in China, Nature Sustainability, 3, 1005-1011, 10.1038/s41893-020-0581-y, 2020.

Hegarty, J., Mao, H., and Talbot, R.: Synoptic controls on summertime surface ozone in the northeastern United States, Journal of Geophysical Research: Atmospheres, 112, https://doi.org/10.1029/2006JD008170, 2007.

465 Huang, X., Ding, A., Gao, J., Zheng, B., Zhou, D., Qi, X., Tang, R., Wang, J., Ren, C., Nie, W., Chi, X., Xu, Z., Chen, L., Li, Y., Che, F., Pang, N., Wang, H., Tong, D., Qin, W., Cheng, W., Liu, W., Fu, Q., Liu, B., Chai, F., Davis, S. J., Zhang, Q., and He, K.: Enhanced secondary pollution offset reduction of primary emissions during COVID-19 lockdown in China, National Science Review, 8, nwaa137, 10.1093/nsr/nwaa137, 2021.

Huth, R., Beck, C., Philipp, A., Demuzere, M., Ustrnul, Z., Cahynová, M., Kyselý, J., and Tveito, O. E.: Classifications of
470 Atmospheric Circulation Patterns, Annals of the New York Academy of Sciences, 1146, 105-152, https://doi.org/10.1196/annals.1446.019, 2008.

Jiang, N., Scorgie, Y., Hart, M., Riley, M. L., Crawford, J., Beggs, P. J., Edwards, G. C., Chang, L., Salter, D., and Virgilio, G. D.: Visualising the relationships between synoptic circulation type and air quality in Sydney, a subtropical coastal-basin environment, International Journal of Climatology, 37, 1211-1228, https://doi.org/10.1002/joc.4770, 2017.

475 Jin, H., Chen, X., Zhong, R., and Liu, M.: Influence and prediction of PM2. 5 through multiple environmental variables in China, Sci. Total Environ., 849, 157910, 2022.

Knote, C., Tuccella, P., Curci, G., Emmons, L., Orlando, J. J., Madronich, S., Baró, R., Jiménez-Guerrero, P., Luecken, D., and Hogrefe, C.: Influence of the choice of gas-phase mechanism on predictions of key gaseous pollutants during the AQMEII phase-2 intercomparison, Atmos. Environ., 115, 553-568, 2015.

480 Kohonen, T.: A simple paradigm for the self-organized formation of structured feature maps, Competition and Cooperation in Neural Nets: Proceedings of the US-Japan Joint Seminar held at Kyoto, Japan February 15–19, 1982, 248-266,

Le, T., Wang, Y., Liu, L., Yang, J., Yung, Y. L., Li, G., and Seinfeld, J. H.: Unexpected air pollution with marked emission reductions during the COVID-19 outbreak in China, Science, 369, 702-706, 2020.

Lelieveld, J., Evans, J. S., Fnais, M., Giannadaki, D., and Pozzer, A.: The contribution of outdoor air pollution sources to
485 premature mortality on a global scale, Nature, 525, 367-371, 10.1038/nature15371, 2015.

Lewis, A. B. and Keim, B. D.: A hybrid procedure for classifying synoptic weather types for Louisiana, USA, International Journal of Climatology, 35, 4247-4261, https://doi.org/10.1002/joc.4283, 2015.

Li, H., Cheng, J., Zhang, Q., Zheng, B., Zhang, Y., Zheng, G., and He, K.: Rapid transition in winter aerosol composition in Beijing from 2014 to 2017: response to clean air actions, Atmos. Chem. Phys., 19, 11485-11499, 10.5194/acp-19-11485-2019,
490 2019a.

Li, K., Jacob, D. J., Liao, H., Zhu, J., Shah, V., Shen, L., Bates, K. H., Zhang, Q., and Zhai, S.: A two-pollutant strategy for improving ozone and particulate air quality in China, Nature Geoscience, 12, 906-910, 10.1038/s41561-019-0464-x, 2019b.

Li, X., Zhao, B., Zhou, W., Shi, H., Yin, R., Cai, R., Yang, D., Dällenbach, K., Deng, C., Fu, Y., Qiao, X., Wang, L., Liu, Y., Yan, C., Kulmala, M., Zheng, J., Hao, J., Wang, S., and Jiang, J.: Responses of gaseous sulfuric acid and particulate sulfate to
495 reduced SO2 concentration: A perspective from long-term measurements in Beijing, Sci. Total Environ., 721, 137700, https://doi.org/10.1016/j.scitotenv.2020.137700, 2020.

Liao, H., Chang, W., and Yang, Y.: Climatic effects of air pollutants over China: A review, Advances in Atmospheric Sciences, 32, 115-139, 2015.

Liao, Z., Gao, M., Sun, J., and Fan, S.: The impact of synoptic circulation on air quality and pollution-related human health in
500 the Yangtze River Delta region, Sci. Total Environ., 607-608, 838-846, https://doi.org/10.1016/j.scitotenv.2017.07.031, 2017.

Liu, J., Wang, L., Li, M., Liao, Z., Sun, Y., Song, T., Gao, W., Wang, Y., Li, Y., and Ji, D.: Quantifying the impact of synoptic circulation patterns on ozone variability in northern China from April to October 2013–2017, Atmospheric Chemistry and Physics, 19, 14477-14492, 2019.

Liu, Y., Wang, T., Stavrakou, T., Elguindi, N., Doumbia, T., Granier, C., Bouarar, I., Gaubert, B., and Brasseur, G. P.: Diverse response of surface ozone to COVID-19 lockdown in China, Sci. Total Environ., 789, 147739, https://doi.org/10.1016/j.scitotenv.2021.147739, 2021.

Lundberg, S. M., Erion, G., Chen, H., DeGrave, A., Prutkin, J. M., Nair, B., Katz, R., Himmelfarb, J., Bansal, N., and Lee, S.-I.: From local explanations to global understanding with explainable AI for trees, Nature machine intelligence, 2, 56-67, 2020.

Lv, Z., Wang, X., Deng, F., Ying, Q., Archibald, A. T., Jones, R. L., Ding, Y., Cheng, Y., Fu, M., Liu, Y., Man, H., Xue, Z., He, K., Hao, J., and Liu, H.: Source–Receptor Relationship Revealed by the Halted Traffic and Aggravated Haze in Beijing during the COVID-19 Lockdown, Environ. Sci. Technol., 54, 15660-15670, 10.1021/acs.est.0c04941, 2020.

Ma, T., Duan, F., Ma, Y., Zhang, Q., Xu, Y., Li, W., Zhu, L., and He, K.: Unbalanced emission reductions and adverse meteorological conditions facilitate the formation of secondary pollutants during the COVID-19 lockdown in Beijing, Sci. Total Environ., 838, 155970, 2022.

Miao, Y., Guo, J., Liu, S., Liu, H., Li, Z., Zhang, W., and Zhai, P.: Classification of summertime synoptic patterns in Beijing and their associations with boundary layer structure affecting aerosol pollution, Atmospheric Chemistry and Physics, 17, 3097-3110, 2017.

Nie, D., Shen, F., Wang, J., Ma, X., Li, Z., Ge, P., Ou, Y., Jiang, Y., Chen, M., and Chen, M.: Changes of air quality and its associated health and economic burden in 31 provincial capital cities in China during COVID-19 pandemic, Atmospheric Research, 249, 105328, 2021.

Pope, R. J., Savage, N. H., Chipperfield, M. P., Ordóñez, C., and Neal, L. S.: The influence of synoptic weather regimes on UK air quality: regional model studies of tropospheric column NO_2, Atmos. Chem. Phys., 15, 11201-11215, 10.5194/acp-15-11201-2015, 2015.

Shen, F., Zhang, L., Jiang, L., Tang, M., Gai, X., Chen, M., and Ge, X.: Temporal variations of six ambient criteria air pollutants from 2015 to 2018, their spatial distributions, health risks and relationships with socioeconomic factors during 2018 in China, Environ. Int., 137, 105556, https://doi.org/10.1016/j.envint.2020.105556, 2020.

Shen, F., Hegglin, M. I., Luo, Y., Yuan, Y., Wang, B., Flemming, J., Wang, J., Zhang, Y., Chen, M., Yang, Q., and Ge, X.: Disentangling drivers of air pollutant and health risk changes during the COVID-19 lockdown in China, npj Climate and Atmospheric Science, 5, 54, 10.1038/s41612-022-00276-0, 2022.

Shu, L., Wang, T., Han, H., Xie, M., Chen, P., Li, M., and Wu, H.: Summertime ozone pollution in the Yangtze River Delta of eastern China during 2013–2017: Synoptic impacts and source apportionment, Environ. Pollut., 257, 113631, https://doi.org/10.1016/j.envpol.2019.113631, 2020.

Su, T., Li, Z., Zheng, Y., Luan, Q., and Guo, J.: Abnormally Shallow Boundary Layer Associated With Severe Air Pollution During the COVID-19 Lockdown in China, Geophys. Res. Lett., 47, e2020GL090041, https://doi.org/10.1029/2020GL090041, 2020.

Sun, Y., Lei, L., Zhou, W., Chen, C., He, Y., Sun, J., Li, Z., Xu, W., Wang, Q., Ji, D., Fu, P., Wang, Z., and Worsnop, D. R.: A chemical cocktail during the COVID-19 outbreak in Beijing, China: Insights from six-year aerosol particle composition measurements during the Chinese New Year holiday, Sci. Total Environ., 742, 140739, https://doi.org/10.1016/j.scitotenv.2020.140739, 2020.

Wang, H., Huang, C., Tao, W., Gao, Y., Wang, S., Jing, S., Wang, W., Yan, R., Wang, Q., and An, J.: Seasonality and reduced nitric oxide titration dominated ozone increase during COVID-19 lockdown in eastern China, Npj Climate and Atmospheric Science, 5, 24, 2022.

Wang, J., Lei, Y., Chen, Y., Wu, Y., Ge, X., Shen, F., Zhang, J., Ye, J., Nie, D., Zhao, X., and Chen, M.: Comparison of air pollutants and their health effects in two developed regions in China during the COVID-19 pandemic, J. Environ. Manage., 287, 112296, https://doi.org/10.1016/j.jenvman.2021.112296, 2021.

Wang, P., Chen, K., Zhu, S., Wang, P., and Zhang, H.: Severe air pollution events not avoided by reduced anthropogenic activities during COVID-19 outbreak, Resources, Conservation and Recycling, 158, 104814, https://doi.org/10.1016/j.resconrec.2020.104814, 2020.

Wang, X., Manning, W., Feng, Z., and Zhu, Y.: Ground-level ozone in China: distribution and effects on crop yields, Environ. Pollut., 147, 394-400, 2007.

Wang, Z. and Bovik, A. C.: Mean squared error: Love it or leave it? A new look at signal fidelity measures, IEEE signal processing magazine, 26, 98-117, 2009.

Weng, X., Forster, G., and Nowack, P.: A machine learning approach to quantify meteorological drivers of ozone pollution in China from 2015 to 2019, Atmospheric Chemistry and Physics, 22, 8385-8402, 2022.

555 Weng, X., Li, J., Forster, G. L., and Nowack, P.: Large modeling uncertainty in projecting decadal surface ozone changes over city clusters of China, Geophys. Res. Lett., 50, e2023GL103241, 2023.

WHO: WHO Coronavirus Disease (COVID-19) Dashboard, 2022.

Xiao, Q., Chang, H. H., Geng, G., and Liu, Y.: An ensemble machine-learning model to predict historical PM2. 5 concentrations in China from satellite data, Environ. Sci. Technol., 52, 13260-13269, 2018.

560 Xu, J., Ge, X., Zhang, X., Zhao, W., Zhang, R., and Zhang, Y.: COVID-19 Impact on the Concentration and Composition of Submicron Particulate Matter in a Typical City of Northwest China, Geophys. Res. Lett., 47, e2020GL089035, https://doi.org/10.1029/2020GL089035, 2020.

Zhan, C.-c., Xie, M., Fang, D.-x., Wang, T.-j., Wu, Z., Lu, H., Li, M.-m., Chen, P.-l., Zhuang, B.-l., and Li, S.: Synoptic weather patterns and their impacts on regional particle pollution in the city cluster of the Sichuan Basin, China, Atmos.

565 Environ., 208, 34-47, 2019.

Zhang, M., Wu, D., and Xue, R.: Hourly prediction of PM 2.5 concentration in Beijing based on Bi-LSTM neural network, Multimedia Tools and Applications, 80, 24455-24468, 2021.

Zhang, Y., Mao, H., Ding, A., Zhou, D., and Fu, C.: Impact of synoptic weather patterns on spatio-temporal variation in surface O3 levels in Hong Kong during 1999–2011, Atmos. Environ., 73, 41-50, 2013.

570 Zhang, Y., Ding, A., Mao, H., Nie, W., Zhou, D., Liu, L., Huang, X., and Fu, C.: Impact of synoptic weather patterns and inter-decadal climate variability on air quality in the North China Plain during 1980–2013, Atmos. Environ., 124, 119-128, 2016.

Zheng, M., Yan, C., Wang, S., He, K., and Zhang, Y.: Understanding PM2.5 sources in China: challenges and perspectives, National Science Review, 4, 801-803, 10.1093/nsr/nwx129, 2017.

575